# A system for in vivo on-demand ultra-low field Overhauser-enhanced 3D-Magnetic resonance imaging.

Dahmane Boudries, Philippe Massot, Elodie Parzy, Seda Seren, Philippe Mellet, Jean-Michel Franconi, Sylvain Miraux, Eric Bezançon, Sylvain R.A. Marque, Gérard Audran, et al.

# A system for *In vivo* On-Demand Ultra-Low Field Overhauser-enhanced 3D-Magnetic Resonance Imaging.

Dahmane Boudries[1], Philippe Massot[1], Elodie Parzy[1], Seda Seren[1], Philippe Mellet[1,5], Jean-Michel Franconi[1], Sylvain Miraux[1], Eric Bezançon[1], Sylvain R.A. Marque[2], Gérard Audran[2], Markus Muetzel[3], Stefan Wintzheimer[3], Florian Fidler[4], Eric Thiaudiere[1*]

[1] Univ. Bordeaux, CNRS, CRMSB, UMR 5536, F-33000 Bordeaux, France
[2] Aix-Marseille University, CNRS, ICR, UMR 7273, F-13013 Marseille, France
[3] Pure Devices GmbH, 97222 Rimpar, Germany
[4] Würzburg University Fraunhofer IIS D-97074 Würzburg, Germany
[5]INSERM, Bordeaux
* Corresponding Author : Prof E. Thiaudiere, Magnetic Resonance of Biological Systems, UMR 5536 CNRS – University of Bordeaux - Campus Carreire – 146 rue Leo Saignat F-33076 Bordeaux Cedex

Credit authorship contribution statement

D. Boudries: Investigation, Writing, Review & Editing. P. Massot: Conceptualization, Investigation, Funding acquisition, Project administration. E. Parzy: Conceptualization, Investigation, Review & Editing. Seda Seren: Investigation. P. Mellet: Conceptualization, Investigation. J-M Franconi: Conceptualization, Investigation, Funding acquisition, Project administration. S. Miraux : Project Administration. Eric Bezançon : Investigation. S.R.A. Marque: Conceptualization, Investigation. G. Audran : Conceptualization, Investigation. Markus Muetzel: Conceptualization, Investigation. Stefan Wintzheimer: Conceptualization, Investigation. Florian Fidler : Conceptualization, Investigation. E. Thiaudiere: Conceptualization, Investigation, Formal analysis, Writing – Review & Editing.

Declaration of Competing Interest

The authors declare that they have no known competing financial interests or personal relationships that could have appeared to influence the work reported in this paper.

Keywords

Ultra-low field
Dynamic Nuclear Polarization
3D-MRI
Nitroxide

Acknowledgments

This project has received funding from the European Union's Horizon 2020 research and innovation programme under grant agreement No 863099. The funding sources had no involvement in the collection, analysis and interpretation of data; in the writing of the report

and in the decision to submit the article for publication.


## Abstract

Development of very-low field MRI is an active area of research. It aims at reducing operating costs and improve portability. However, the signal-to-noise issue becomes prominent at ultra-low field (<1 mT), especially for molecular imaging purposes that addresses specific biochemical events. In the context of preclinical molecular MRI of abnormal proteolysis the paper describes a MRI system able to produce Overhauser-enhanced MR images in living rats through in situ Dynamic Nuclear Polarization at 206 µT using stable and non-toxic nitroxides. In parallel conventional images are generated at 206 µT following pre-polarization at 20 mT. Results show that nitroxides are visualized in 3D within a few minutes in the lungs, kidneys and bladder post-administration. This system will be used for molecular imaging of inflammation using protease-specific nitroxide probes.


## Introduction

MRI is a reference imaging modality for a variety of medical indications, thanks to its high natural contrasts, anatomical resolution and innocuousness. A lot of instrumental and technological developments made it available worldwide at 1.5-3 T operating fields while there is an increasing interest for higher magnetic fields (7 T or higher) opening new exploration opportunities of human anatomy and diagnoses of pathologies [1-2]

These advances are accompanied with progress in molecular imaging that enables the visualization of specific biological processes. This emerging approach may play an important role in the development of personalized medicine, allowing early diagnosis and monitoring of therapeutic treatments. To cope with the growing need for this medicine, MRI is an appropriate candidate provided the sensitivity issue is addressed.

In parallel an increasing interest to low, very-low, ultra-low field MRI is in progress [3]. Lower fields could be preferred for they allow higher $T_1$ contrasts, lower sensitivity to artifacts and cost-efficiency for instrument design and maintenance [4]. However the sensitivity issue is undeniable, especially at ultra-low field (<1 mT), which prompted the use of hypersensitive detectors such as SQUID (Superconducting Quantum Interference Device) [5-7]. Despite quite appealing, such approaches still require development particularly if applied to molecular imaging of diluted molecular species.

One way to perform molecular MRI is to use hyperpolarized substances that allow the magnetization transfer to nuclei such as noble gases [8,9] or parahydrogen [10]. This strategy not only allows huge gains in sensitivity, but also provides biochemical specificity for metabolic imaging, as demonstrated at high fields [11] and in clinical practice with $^{13}C$-labeled substrates [12]. The limitation is the need of an external preparation of the hyperpolarized sample and the short *in-situ* time window for MRI. Another modality, Overhauser-enhanced MRI (OMRI) [13,14] uses electron paramagnetic resonance (EPR) of free radicals to carry out polarization transfer to protons at their vicinity. This allows *in situ*

on-demand increase in NMR signal. OMRI was used i*n vivo* for assessment of redox status [15] or oximetry [16-18] or free radical biodistribution [19] in rodents.

NMR signal enhancement through Overhauser effect would be very useful when employed to target enzymatic activities *in vivo*. More specifically protease imaging is clinically relevant because alterations in proteolytic systems result in various pathologies [20] such as pancreatitis [21], solid tumours [22], renal inflammation [23,24], cystic fibrosis [25] and chronic obstructive pulmonary disease (COPD) [26]. Recent OMRI developments demonstrated the ability to detect the neutrophil elastase activity associated with inflammation in lungs of living mice [27] using a novel protease-specific nitroxide [28] at low-field (0.2 T). At this field the EPR irradiation occurred at 5.4 GHz range, which limited the use of this approach to mice, because of penetration depth issues. Moreover, tissue heating would also happen at high EPR frequency, thus impeding the translation of this OMRI approach to larger animals or humans.

In this respect, a significant reduction in EPR frequency, hence in magnetic field, is needed for safety reasons [29]. Other benefits of very low or ultra-low fields are portability and cost-efficiency [30]. A recent Overhauser-enhanced spectroscopy work established the feasibility of measuring a neutrophil elastase activity at ultra-low field (Earth's field, 44 µT) *in vitro* using the same radical probe [31]. A further advantage of very low-fields is the occurrence of one or more hyperfine couplings which provide large Overhauser enhancements with nitroxides [32]. The obvious extension of this work is to perform OMRI of enzymatic activity *in vivo* in large animals. The first step is to implement a complete OMRI system operating at ultra-low fields on rat-sized animals. The system should also be able to acquire conventional MR images at higher fields. The present study describes i) the OMRI setup operating at 206 µT with possible prepolarization at 20 mT, ii) *in vitro* assessment of Overhauser effects and iii) *in vivo* biodistribution of injected 3-line nitroxides in living rats.

## Theoretical model

In this section a brief reminder is given to describe the basic principles to calculate the EPR frequencies for a 3-line nitroxides and the Overhauser enhancement factors. Details are given in [32].

We consider a simple case of intramolecular hyperfine coupling between unpaired electron spin S = ½ and nuclear nitrogen spin K = 1 ($^{14}$N). If the $B_0$ magnetic field is aligned along the z-axis, the Hamiltonian of the system can be described by :

$$\widehat{H_0} = \omega_e \widehat{S_z} + \omega_N \widehat{K_z} + a_N \left[ \widehat{S_z}\widehat{K_z} + \frac{1}{2}\left(\widehat{S_+}\widehat{K_-} + \widehat{S_-}\widehat{K_+}\right)\right]$$

The z-subscript terms represent the populations of the states (Zeeman interaction with the main field $B_0$), the terms in (+) and (-) represent the raising and lowering between states of different energy, and the ω the angular frequencies proportional to $B_0$. Coefficient $a_N$ is the electron-nucleus hyperfine coupling constant and the bracketed members represent the coupling Hamiltonians. Experimentally, $a_N$ is 45 MHz in frequency unit.

Solving the above equation allows to find the states and energies of each state of the electron and the transition probabilities between states.

The analytical resolution gives 6 eigenstates. There is a certain number of possible transitions π and σ, with different probability values. In our case we are interested in π transitions (where the EPR field is perpendicular to $B_0$), more specifically $\pi_{1\text{-}6}$ between states 1 and 6. The expression of the Dynamic Nuclear Polarization factor (DNPF) is defined as:

$$DNPF = \varepsilon - 1 = \rho f \left[\frac{\langle S_z\rangle - S_0}{I_0}\right] \quad \text{with} \quad \varepsilon = \frac{\langle I_z\rangle}{I_0}$$

and

$$\langle S_z\rangle - S_0 = \sum_i \langle i|S_z|i\rangle\,(n_i - n_i^0)$$

where ε is the enhancement factor, $\langle I_z\rangle$ the proton polarization under EPR irradiation, $I_0$ the equilibrium proton polarization, ρ is the electron-nucleus coupling factor, f is the leakage factor, $n_i$ and $n^0_i$ the populations of the i-state respectively without and with the saturation of the transition. It can be derived :

$$DNPF_{ij} = \frac{\rho f s}{n\gamma_I B_0}\left(E_i - E_j\right)\left(\langle i|S_z|i\rangle - \langle j|S_z|j\rangle\right).W_{ij}$$

where $W_{ij}$ is the transition probabilities, $\gamma_I$ the proton gyromagnetic ratio and n = (2S + 1)(2 K + 1), n = 6 in the present case. The EPR saturation factor **s** is defined as 1- $\langle S_z\rangle/S_0$. Fig.1 shows the maximum DNPF expected from a 3-line nitroxide with $a_N$ = 45.4 MHz, s = 1 (perfect EPR saturation), f = 1 (proton longitudinal relaxation only due to the presence of the electron spin) and ρ = 0.5 (pure dipolar coupling). The frequency range corresponds to the two most efficient lines ($\pi_{4\text{-}5}$ and $\pi_{1\text{-}6}$). The DNPF of $\pi_{2\text{-}5}$ and $\pi_{3\text{-}6}$ transitions (-16 and -11, respectively) can be neglected.

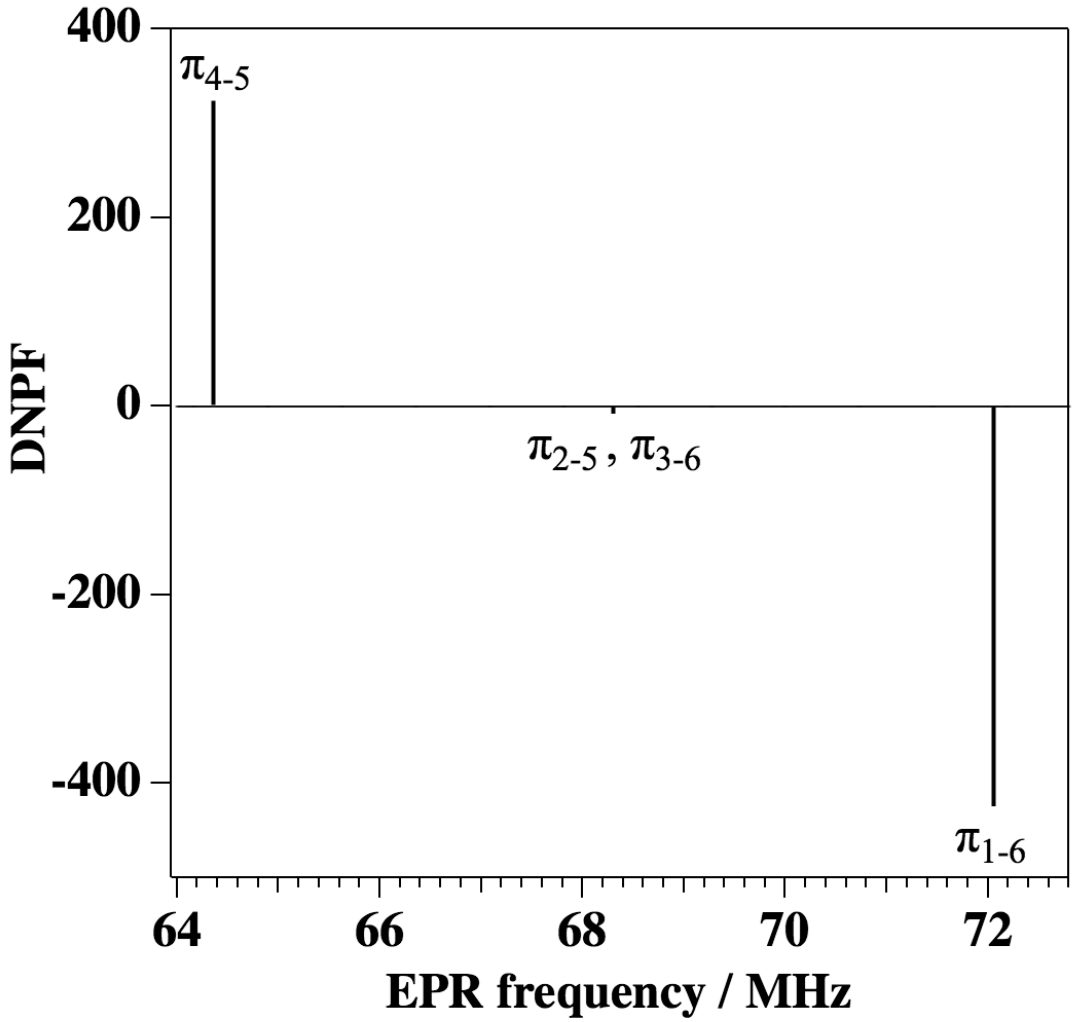


*Figure 1: Simulated maximum DNP factors at 206 µT in the 70 MHz range relative to $\pi_{ij}$ transitions with s = 1, f = 1 and ρ = 0.5. Hyperfine coupling constant: $a_N$ = 16.2 G or 45.4 MHz*

Only the $\pi_{1\text{-}6}$ line shall be considered in the next experiments because of its highest DNPF (-447) and its negative value that induces a typical 180-degree phase shift in the proton NMR signal.

## Materials and methods

### Hardware

The system was composed of a 3-axis $B_0$ cage, a pre-polarization coil, a 3-axis $B_0$ gradient set, a transmit-receive $^1$H RF-coil, a transmit-only EPR coil, a pre-polarization driver, independent transmitter channels for proton and electron, a proton receiver channel, and a system control unit. Details are given below.

1. $B_0$ cage. It consisted of three orthogonal sets of two quadratic coils in a Helmholtz arrangement to create a static magnetic field in any direction up to approximately 206 µT. It was also used to compensate at the same time the residual magnetic field components (Earth's magnetic field or any static field present at the experimental location).

2. Pre-polarization coil. It was a switchable solenoid coil oriented along x-direction that creates a magnetic field of 20 mT at its center for 8 A current. The maximum current was 20 A. The inner diameter was 150 mm with a length of 160 mm.

3. Gradient system. It was a 3-channel gradient system consisting of coils wound on a cylinder with an inner diameter of 280 mm and a length of 370 mm. The maximum gradient strengths in each direction were : $G_X$ = 488 µT/m, $G_Y$ = 647 µT/m and $G_Z$ = 238 µT/m. Other details can be found in [33]. The gradient coil was also used for linear shimming.

4. Transmit and receive $^1$H coil. The receiver coil was a home-made second-order axial gradiometer made of 3 elements, *i.e.* a central 110 mm long and 80 mm inner diameter solenoid (inductance : 44 mH) and two coaxial counter-field shorter solenoids positioned symmetrically at each end, each 20 mm in length and 110 mm in diameter (inductance : 22.2 mH each). Capacitive tuning was carried out at 8.79 kHz. The quality factor was 24. The transmitter was a solenoid (20 turns) wound around the central receiver solenoid. The NMR coil holder was modeled with the rhino7 software (McNeel Europe, Barcelona, Spain) then printed with Form3 3D-printer (Formlabs, Paris, France).

5. EPR coil. A low-pass birdcage transmit coil (8-legs, D = 62 mm, L = 95 mm, inductance : 188 nH) was designed using Comsol® Multiphysics (Grenoble, France), to operate at 72 MHz with linear polarization. Coil tuning and matching were carried out with fixed non-magnetic capacitors C = 39 pF on legs, and a variable capacitor, 0.5-8 pF at end-rings, all non-magnetic from Exxelia® (Pessac, France). As with the NMR coil, the support used for the DNP coil was modeled with the rhino7 software then printed with Form3. The quality factor was about 60, the power needed to saturate EPR transitions was 15 Watts.

6. Pre-polarization driver. A standard power supply with voltage and current controls was used. It fed the pre-polarization coil through a power switch actively controlled by the console. The whole pre-polarization process was carried out in three sequential steps : i) fast ramp-up to 20 mT along the x-axis with a constant current supply regulated at 8 amperes ; ii) a first fast ramp-down step (6 ms) to reach a value of few mT along the x-axis; iii) a slow ramp-down step to ensure the adiabatic switch to 206 µT along the z-axis within 60 ms. This last step allowed the conservation of the proton magnetization produced by the first pre-polarization step. Additionally, a software-controlled delay of few milliseconds allowed any residual pre-polarization field to vanish before starting the NMR acquisition.

7. EPR channel. The RF wave was generated by a console using a direct digital synthesizer (Pure Devices, Rimpar, Germany). RF frequency, amplitude and pulse duration were controlled within OpenMatlab console software. Additionally, a manual step attenuator, 0-63dB in 1dB steps (RLC Electronics, New-York, USA) was used to control the final power delivered to the coil. The signal was used as an input to an RF amplifier (bandwidth 1-180 MHz, power : 100 Watts) in either pulsed or continuous mode (RFPA, Artigues-près-Bordeaux, France).

8. Control Unit. It consisted of two MRI consoles from Pure Devices (Rimpar, Germany), one for transmit and receive of the low frequency RF signal as well as gradient control, one for controlling the $B_0$-cage. The transmit/receive console was modified to be able to work on low frequency signals. Both consoles were synchronized to allow concurrent real-time control.

The gradient control drove a modified 4-channel gradient amplifier matching the characteristics of the gradient systems. The $B_0$-cage was driven by another modified gradient amplifier capable of keeping the current stable enough to perform MR experiments in the artificially generated ultra-low field.
The consoles were driven by a 12V DC power supplies, generating low disturbances.
Additionally, the setup contained batteries to supply the line driver and the preamplifier, to limit noise pickup in the early signal conditioning stages. The consoles were connected to the computer via USB cables.

In addition, an aluminium shielding (diameter 250 mm, length 500 mm, thickness 4 mm) has been inserted to limit unwanted RF sources at the observation $^1$H NMR frequency, like power lines harmonics.

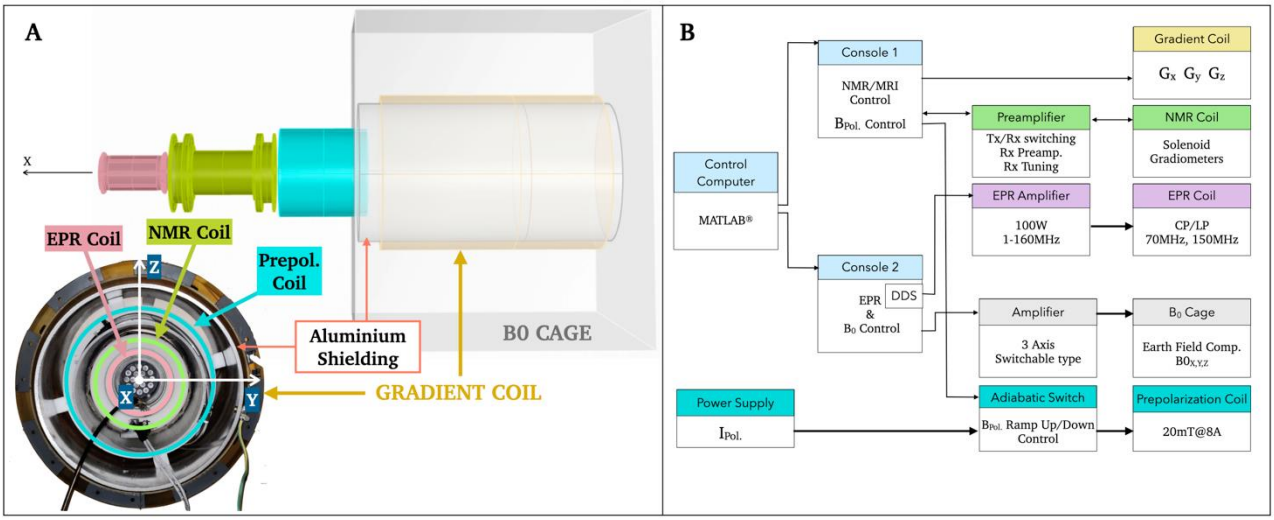


*Figure 2: Overall scheme of the instrument. (A) A schematic exploded side-view of the system illustrated by a picture of the front side. (B) Logical connections between the different elements.*

Chemicals

TOPCA (3-Carboxy-2,2,5,5-tetramethyl-3-pyrrolin-1-yloxy) and 3-Carboxy-PROXYL ((3R)-1-hydroxy-2,2,5,5-tetramethylpyrrolidine-3-carboxylate, 3CP) were purchased from Sigma-Aldrich (Saint-Quentin-Fallavier, France). Aqueous solutions of nitroxides (1-50 mL) in the millimolar range were prepared and buffered at pH=7.4. The $a_N$ values were 16.2 G (45.4 MHz) and 16.15 G (45.26 MHz) for TOPCA and 3CP, respectively.

Phantoms

For spectroscopic experiments, 50-mL PTFE cylindrical vials (80 mm in length, 30 mm in diameter) were filled with TOPCA in buffered water.

For 3D imaging a multi-compartment holder was 3D-printed. It housed 19 cylindrical vials (0.5 mL, 5 mm in diameter and 3 cm in length) filled with TOPCA in buffer. TOPCA concentrations were in the 0-1 mM range.

Animal preparation

Wistars rats (female, 8 weeks, 250 ± 20 g) were anesthesized with intraperitoneal injection of ketamine-xylazine (75-100 mg/kg / 10 mg/kg). For kidney/bladder imaging they were intravenously injected with 1.5 ml of 200 mM TOPCA. For lung imaging, they were instilled intratracheally with 100 µl of 100 mM 3CP. For intravenous injection a catheter was introduced in the tail vein, then the injection was done manually for 1 minute during the OMRI acquisition.

For lung instillation, a MicroSprayer Syringe Assembly for Rat Model IA-1C-R from Penn-Century (Wyndmoor, PA) was used. Rats were positioned in supine position in a home-made bed. This bed was equipped with water circulation for temperature regulation. An optical fiber temperature probe was installed in mouth. A respiratory probe was attached to the abdomen. All procedures performed during this study were approved by the Animal study Ethics Committee (authorization # B33-063-926) of the University of Bordeaux.

Pulse sequences and acquisition protocols

All sequences included a preparation step, either pre-polarization by switching the polarization field to 20 mT, or EPR irradiation at 206 µT. Then the $^{1}$H NMR experiment (relaxation times measurements, spectroscopy or imaging) was conducted at 206 µT after 15 ms switching time. In OMRI experiments EPR irradiation started 5 seconds before the NMR experiment and was applied continuously throughout the whole acquisition. The EPR frequency was adjusted as a function of both the $B_0$ field and the electron-nucleus hyperfine coupling constant. The NMR frequency was 8.79 kHz.

Spectroscopy measurements

Spin-echo acquisitions were carried out in vitro as already described [31]. When used, pre-polarization was applied for 5 seconds (including adiabatic switch-off) followed by 15 ms switching time, prior to the NMR sequence. RF pulse lengths were 2.4 ms and 4.8 ms for $\pi/2$ and $\pi$ nutation angles, respectively. TR/TE were 565/450 ms with 225 ms readout time. The number of average was 1 and the total acquisition time was 5.565 s respectively. For the DNP experiments the EPR irradiation time was 5 seconds keeping the same TR/TE. In order to acquire the DNPF line for the $\pi_{1\text{-}6}$ transition the EPR frequency was varied from 69 to 77 MHz with 0.5 MHz steps, which necessitated EPR coil tuning. The same experiments were repeated without EPR so as to calculate :

$$\varepsilon = \frac{S_{DNP}\, B_{POL}}{S_{POL}\, B_{ULF}}$$

where $S_{DNP}$ is the NMR signal (SNR) measured using EPR irradiation, $S_{pol}$ is the NMR signal (SNR) with magnetic pre-polarization. $B_{pol}$ is the pre-polarization field (20 mT), and $B_{ULF}$ the ultra-low field produced by $B_0$ cage (206 µT).

Relaxation measurements at 206 µT.

Longitudinal ($T_1$) relaxation time constants at 206 µT were measured on 50 mL phantoms at various nitroxide concentrations using pre-polarization. The pre-polarization time was fixed to 15 seconds followed by a field switch to 206 µT. Then a lag-time was varied from 90 to 16000 ms prior to a 90° RF-pulse followed by acquisition of the FID. The decrease in signal amplitude as a function of the lag-time time was fitted to a monoexponential function with $T_1$ as time constant. Rough estimate of $T_1$ were also carried out on intact rats with the same protocol. The approximate value of transverse $T_2$ relaxation time constant in the intact rat was measured with a CPMG pulse sequence (inter-echo time : 50 ms, number of echoes : 150) following 0.5 second pre-polarization at 20 mT.

3D Imaging

Three imaging sequences were used depending on the $T_2$ value of phantom or living rats. In all cases, no slice selection was performed and only rectangular (2.5 ms) RF pulses were used. In phantoms, where $T_2$ were in the range of 500-2000 ms (data not shown), either spin echo (TR/TE = 1730/85 ms) or balanced steady-state free precession (bSSFP) (TR/TE = 115/57.5 ms) sequence could be used. Spin-echo was used in the case of magnetic pre-polarization whereas bSSFP was appropriate for DNP under continuous EPR irradiation, keeping the steady-state magnetization. Other parameters for spin-echo with magnetic pre-polarization: resolution 4x4x6 $mm^3$ (read/phase/partition); FOV 72×72×56 $mm^3$, 6 averages, 43 minutes acquisition time and for bSSFP with EPR saturation: resolution 4x4x8 $mm^3$ (read/phase/partition), FOV 72x72x56 $mm^3$, 4 averages with 168 s acquisition time.

For in vivo experiments, where $T_2$ was approximately 90 ms, Zero-echo-time (ZTE) sequence was preferred (TR/TE = 245/0 ms + 13 ms). The 13 ms time corresponds to a dead-time introduced before readout to avoid acquiring the ringing of the receiver coil mainly caused by inductive coupling between the $^1H$ transmit-coil and the receiver coil. The pre-polarization time was 0.5 second because of shorter $T_1$, in the range of 100 ms (data not shown). Other parameters for ZTE: resolution 3×3×6 $mm^3$ (read/phase/partition); FOV 81×81×60 $mm^3$; 1 average; 30 min acquisition time with pre-polarization; In abdomen: 560 s acquisition time with EPR saturation. In lungs: resolution 5.7×5.7×6 $mm^3$ and FOV 80×80×60 $mm^3$, 168 s acquisition time with EPR saturation.

A summary of the imaging acquisition protocols is displayed in Figure 3.

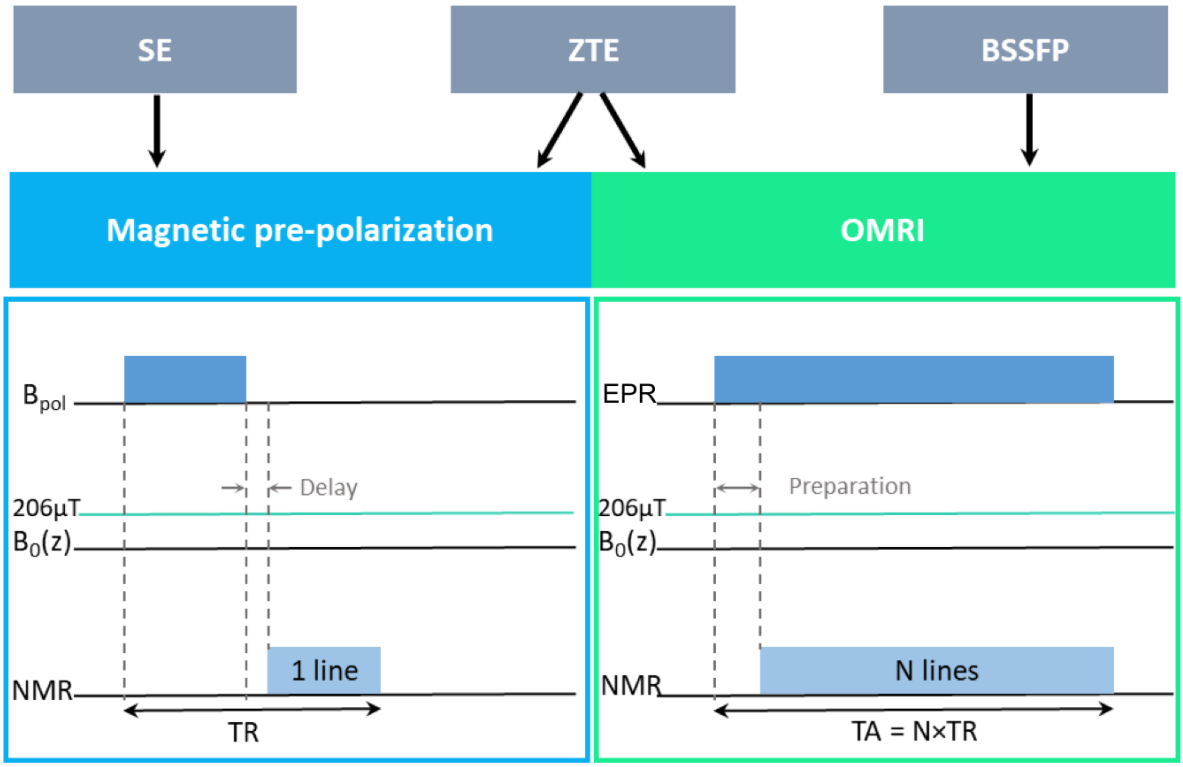


*Figure 3. Acquisition protocols. Spin-echo (SE) and balance steady-state free precession sequences were used* in vitro *only whereas Zero-echo-time (ZTE) was used* in vivo. *In OMRI experiments EPR was applied throughout the acquisition.*

Results

$T_1$ measurements of aqueous solutions of TOPCA at various concentrations with prepolarization at 20 mM allowed an estimation of a longitudinal relaxivity $r_1$ value of $0.75\pm0.05 mM^{-1}s^{-1}$ with a $r_{10}$ value for free water of $0.358 mM^{-1}s^{-1}$. This relaxivity could be used to calculate the leakage factor of TOPCA at 1mM concentration, *i.e.* f = 0.52.

In order to evaluate the efficiency of the system to generate significant Overhauser enhancements over a range of EPR frequency, the DNPF of solution of 1 mM of TOPCA in water was measured from 70 to 77 MHz, which corresponded to the $\pi_{1\text{-}6}$ EPR transition. Results are displayed in Figure 4, where it can be observed negative values for the DNPF resulting from a 180-degree phase shift in the NMR signal as compared with what measured without DNP with pre-polarization. Curve fitting to a Lorentzian EPR line gave an apparent linewidth of 3.5 MHz. The maximal observed DNPF of -218, i.e. 0.49 times the theoretical value of -447 calculated with the product $\rho.f.s = 0.5$ (Fig. 1, see the theoretical section). Taking into account the actual value of f = 0.52 in the measured DNPF spectrum, the observed data correspond to perfect EPR saturation (s = 1) and a coupling factor $\rho = 0.47$.

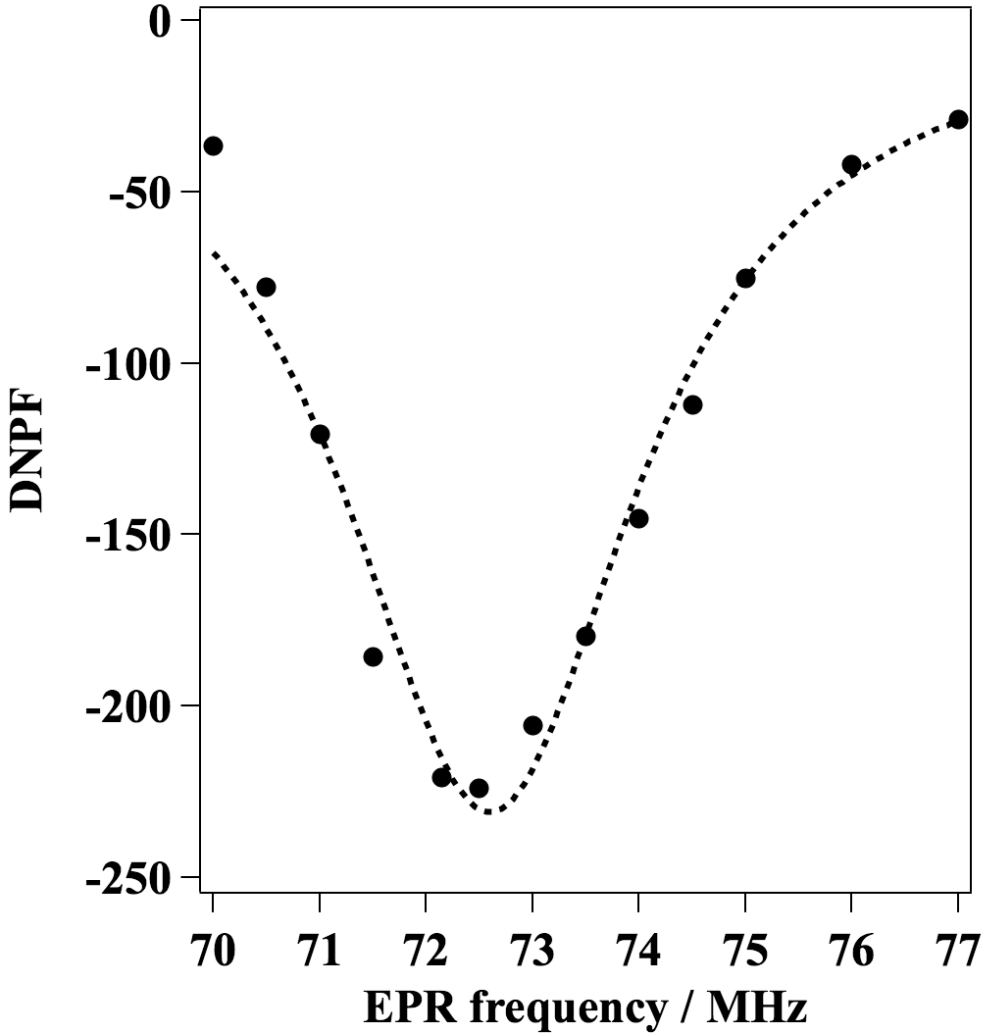


*Figure 4. (data points) Dynamic Nuclear Polarization factor of 1.0 mM TOPCA in water. (dashed line) Curve fit to a Lorentzian function with a linewidth of 3.5 MHz.*

Figure 5 shows a cross-section picture of the phantom made of 19 vials with various TOPCA concentrations and extracted partitions of the 3D images generated either with prepolarization at 20 mT or Overhauser-enhanced images with continuous EPR irradiation at 4-mm in-plane resolution. A spin-echo sequence was used in the first case and a bSSFP for the second case. As a true 3D encoding was performed surface rendering were possible and displayed also in Fig. 5. The $^{1}$H gradiometer was able to provide homogeneous images, as seen in pre-polarized images. Signal variation across the FOV are very likely due to the relaxivity of the nitroxide : indeed the presence of the free radical induced $T_1$ shortening hence an apparent increase in NMR signal at higher nitroxide concentration with a pre-polarization time of 1.5 second only. Signal-to noise ratio (SNR) ranged from 8.5 to 15 for 3D image (with 8.2 SNR for water). In OMR images only TOPCA-containing vials exhibited a significant signal. Signal intensity expectedly was higher for higher nitroxide concentrations because of the role of the leakage factor. The SNR was 7.5 to 19. The EPR field homogeneity was checked in separate experiment (data not shown). Analysis of 3D matrices showed that both the NMR and EPR radiofrequency fields were homogeneous over the partition-encoding direction.

Results in phantoms showed that nitroxide concentration as low as 100 µM could be detected in 3D thus allowing in vivo experiments in rats with comparable FOV. Gross estimates of $T_1$ and $T_2$ of the intact rat were carried out prior preliminary imaging tests. Values of $T_1$ and $T_2$ were *ca*. 110 ms and 90 ms, respectively. Because of $T_2$ limitations the ZTE sequence was therefore used instead of bSSFP or spin echo. Here the goal was to assess the feasibility of nitroxide detection in rat body post-injection or post-instillation. Because of the limited size of the RF coils whole-body imaging was not possible. Three regions were defined : head, chest and abdomen that were separately imaged in 3D using pre-polarization at 20 mT in order to reconstruct an "anatomical" image. In OMRI experiments the abdominal region was chosen to focus on renal elimination in the case of nitroxide injection in the blood stream on one hand and the chest region in the case of intratracheal instillation on the other hand.

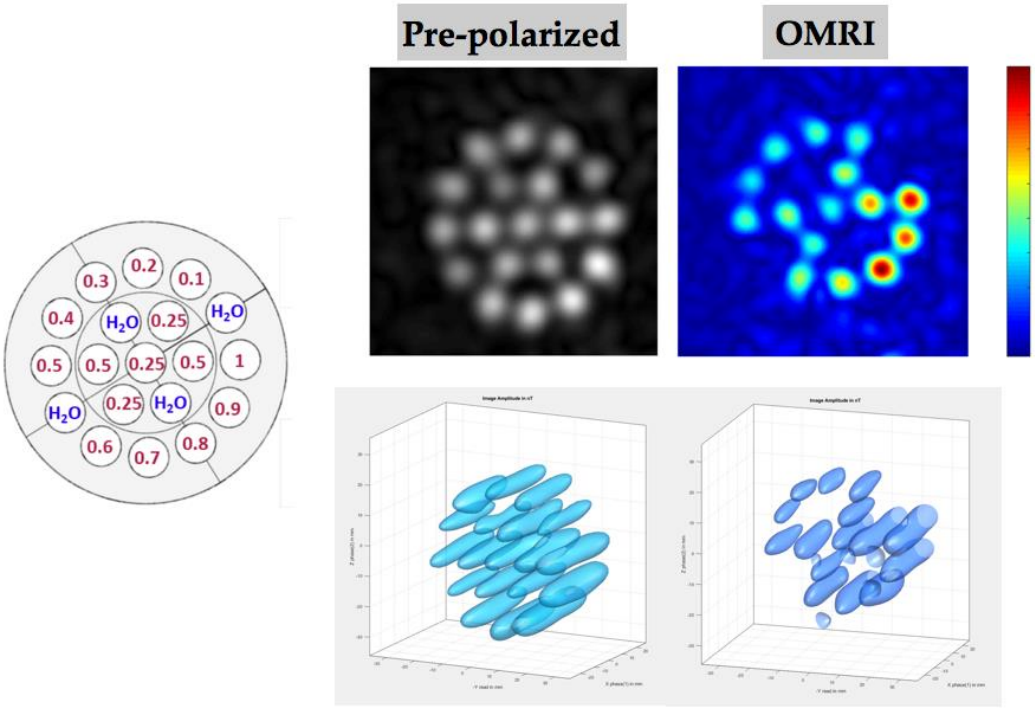


*Figure 5. Sketch of the nitroxide phantom (left) and extracted slices from 3D images with pre-polarization (middle) or Dynamic Nuclear Polarization (Right, linear color scale) and their corresponding isosurface plots for 3D rendering. The red numbers in the left panel indicate nitroxide concentration in millimolar, "$H_2O$" stands for pure water.*

Figure 6 shows extracted slices from the aggregated 3D images for both the anatomical images with pre-polarization and OMRI of a living rat. By juxtaposing the matrices from three separate pre-polarized MRI experiments on different body regions the overall shape of the animal can be clearly distinguished from the head to the hind limbs. The SNR was 8 in the lung region and 19 in the kidney region. The anatomical images were used to approximately register the coordinates of the Overhauser enhanced signal in the presence of a nitroxide. When intravenously injected TOPCA was visible in the kidneys with a SNR of 4 immediately

after the injection as seen in the figure. Hypersignal was also recorded in the bladder region with a SNR of 3. When measured 20 minutes post-injection OMRI on the same rat showed an increase accumulation of TOPCA in the bladder (not shown) with a SNR of 4. In lungs TOPCA was unfortunately not detected by OMRI after instillation. The reasons for that are unclear : it could be either an instillation problem or a rapid elimination of this particular nitroxide in lungs. This is why 3CP was used instead. In Figure 6, a bright spot appeared in OMR images in the lung region. Here there was 2 min lag time between instillation and the beginning of data acquisition. By lowering in-plane resolution the imaging time was reduced to compensate for clearance of the nitroxide in lungs, as already observed in mice at 0.194 T [27]. The SNR was 4 in the displayed image. When the same rat was repositioned 15 minutes later in the abdominal region the OMR image displayed enhanced signal in the bladder (not shown), suggesting the renal elimination of the nitroxide. For the sake of readability, Fig.6 also displays co-registered images of the observed DNP enhancements over the anatomical image.

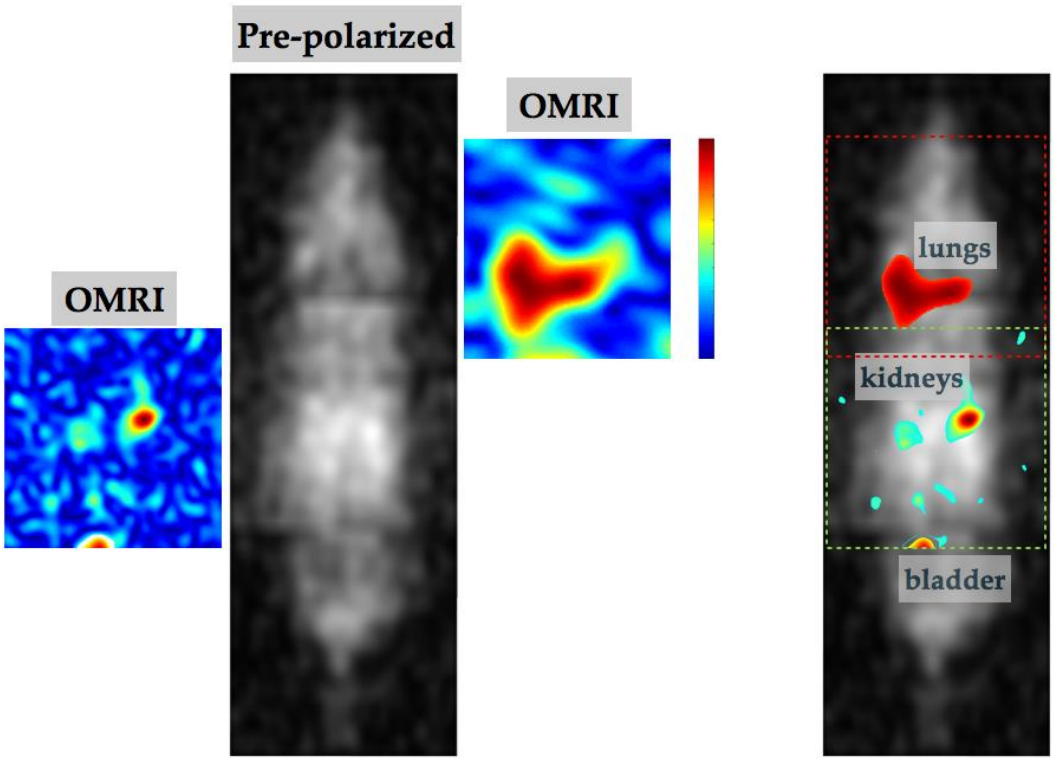


*Figure 6. Pre-polarized (gray scale) and OMR images (linear color scale) at 206µT of a living rat injected or instilled with nitroxides. The whole-body image is the aggregate of 3 matrices. On the right part the higher DNP signals with the same color scale are superimposed to the whole-body image. The red and green boxes correspond to the approximate position of the FOV of OMR images acquired in lung with 3CP instillation and abdomen with TOPCA injection, respectively.*

## Discussion

This paper describes the development of an ultra-low field system able to perform *in situ* DNP-enhanced imaging in large rodents. It might be considered as a strong incremental development of a previous system used for DNP at Earth's field [31]. An obvious benefit of this approach is the needlessness for any external hyperpolarization system. Therefore Overhauser enhancements may be recorded as long as the free radical is present. This system is intended to be used for molecular imaging of abnormal proteolysis in the foreseeable future. The use of ultra-low fields was prompted by the need for higher penetration depth of the EPR waves together with reduced animal heating as compared with the already developed system operating at 0.19 T which was mouse-dedicated [34]. The present system can be considered as intermediate before the construction of a larger system adapted to bigger animals or even humans.

The $B_0$-cage was able to suppress the local 44 µT Earth's field and to generate a constant $B_0$ field at 206 µT. This value was chosen as a tradeoff : indeed the DNPF is expected to be higher at 44 µT but this advantage is partially cancelled by the overlap of EPR π-transitions with positive and negative enhancements [31]. Instead, a slight increase of $B_0$ to 206 µT improve the splitting of positive and negative DNPF lines (Fig. 1) while keeping the benefit of the use of an ultra-low field. Therefore, no circularly polarized wave was necessary to select a given EPR line. Moreover, the use of a wave circularly polarized about the z-axis implies an utterly different orientation of the EPR coil, not compatible with the proposed co-axial alignment of the hardware elements.

This system is able to magnetically pre-polarize the proton spins at 20 mT, which is compulsory for the generation of conventional images. Indeed, the NMR signal without any kind of pre-polarization (magnetic or dynamic) was undetectable. Local field heterogeneity in phantoms or animals was shimmed with the gradient coil. In pure water, $T_2$* as long as 600 ms were observed, corresponding to *ca.* 20 ppm field heterogeneity. In living rats, the apparent $T_2$ and $T_2$* were in the range of 90-100 ms and 70-80 ms, respectively which corresponded to about 50 ppm heterogeneity. Such values constitute a significant improvement if compared with the previous system used for Earth's field DNP [31].

Standard spin-echo or bSSFP MRI could be used in phantoms which $T_2$ were greater than 500 ms. In living animals where $T_2$ and $T_2$* were in the range of 100-70 ms radial imaging was used instead of conventional Cartesian encoding. Interestingly, the very approximate values of $T_1$ and $T_2$ in rats were found in the same range as those already published in Earth's field [35]. ZTE was made inevitable because of long gradient ramp times and low gradient strengths needed at low polarization fields. Moreover, the low receiver bandwidth of the gradiometer (*ca.* 200 Hz) precluded very fast echo sampling. Obviously it must be conceded that both space-resolution and contrasts were poor in pre-polarized images in the living rat with this system. Nevertheless, images were acquired in three dimensions and the whole rat body could be reconstructed from separated 3D acquisitions. Several improvements might be envisioned. For instance, the field generated by the $B_0$-cage was not perfectly stable with observed drifts of ± 8 Hz proton frequency over time. A field-frequency lock procedure could bring a much better stability. Shorter gradient ramp times and Eddy currents compensation would be also beneficial for image quality *in vivo*. Indeed, ramp times lower than 1 ms and readout gradient strengths of about 0.5 mT/m allow Cartesian encoding of a 20 cm FOV at 3 mm resolution with echo times lower than 20 ms and repetition times lower than 50 ms, provided that the dead-time due to the ringing of the receiver coil is suppressed. In vivo, a 64x32x32 matrix for a FOV of 20x10x10 cm would thus be acquired

within 6 minutes with a pre-polarization time of 300 ms. Such acquisition parameters would therefore require both an active decoupling of the transmit and receive NMR coils and an increase in the receiver bandwidth but at the expense of the SNR. This drawback could be mitigated through the use of Deep Learning approaches of noise reduction [4,36]. Deep Learning applied to undersampled data sets could also allow faster acquisition at very low field [37]. In the specific case of ZTE the reduction of the lag time between the RF pulse and the readout would also greatly improve the acquisition of the central k-space data, together with known methods to fill the dead-time gap [38]. It must be kept in mind that a huge improvement in anatomical imaging would be achieved provided signal acquisition were performed at 20 mT (850 kHz) without field cycling down to 206 µT. Still, this would require much higher magnetic field stability than required in the present system.

Preliminary DNP experiments on phantoms allowed to measure the apparent linewidth of the selected EPR line of the TOPCA nitroxide by shifting the EPR frequency. The measured signal enhancement at 72 MHz EPR frequency made it very clear that a nitroxide in the millimolar range was readily detectable. The detection sensitivity was even higher as seen in Fig. 5 where concentrations as low as 0.1 mM was detected in 3D OMR images *in vitro*. Therefore OMRI was thought to be usable *in vivo*, where systemically injected radicals could be highly diluted after biodistribution/elimination processes.

Of note, the use of continuous EPR irradiation for 3 minutes or 10 minutes did not induce any significant animal heating. The Specific Absorption rate (SAR) was estimated from temperature (T) measurement over time (t). The initial slope of the curve (1°C over 10 minutes) was related to the SAR through an average value of the specific heat capacity (3.66 kJ/kg/K) in rodents [39]. The instantaneous SAR-value of 6 W/kg was thus found compatible with *in vivo* studies, especially with additional rest periods between OMRI acquisitions.

*In vivo*, two ways of nitroxide administration were used in order to assess the biodistribution in rats : either instillation in lungs or venous injection. OMRI was performed in 3D and images were co-registered with pre-polarized anatomical images. Importantly, the nitroxides were both detectable in the lungs, the kidneys and the bladder. Such a result is a bedrock for future investigation of protease overexpression under pathological situations. Indeed, inflammation in lung or kidneys triggers huge local protease accumulation, hence strong tissue injury. Owing to the proper use of dedicated protease substrates [40], OMRI in living diseased rats would provide invaluable information on the time course of inflammation process *in situ*, both for basic understanding and anti-protease drug evaluation.

Even though the use of smart nitroxides to assess abnormal enzyme metabolism in Humans is out of the scope of this paper, nitroxide toxicity and dosage are relevant issues in this context. Is was shown by us [34] and others [41,42] that stable nitroxides injected in the blood stream at doses as high as 600 mg/kg were not harmful for rodents, even in the case of repeated experiments. In the specific case of instillation in lungs, the dose was in the range of 8 mg/kg in the present study with no adverse effect. Moreover, a fast renal elimination was observed mostly because such nitroxides are small and water-soluble molecules. Importantly, the chemical structure of the eliminated nitroxides found in the bladder was conserved, which indicated that they can be considered as inert during the elimination process. Such properties could be of great value in the frame of future development of protease imaging in Humans.

Work is in progress to translate this approach to larger animals by manufacturing a human-sized versatile instrument able to produce both conventional MR images with sensible quality and on-demand enzyme activity mapping.

References

[1] Barisano G., Sepehrband F., Ma S., Jann K., Cabeen R., Wang D.J., Toga A.W., Law M. Clinical 7 T MRI: Are we there yet? A review about magnetic resonance imaging at ultra-high field. Br J Radiol. 2019 92(1094) (2019) 20180492. doi: 10.1259/bjr.20180492

[2] Ladd M.E., Bachert P., Meyerspeer M., Moser E., Nagel A.M., Norris D.G., Schmitter S., Speck O., Straub S., Zaiss M. Pros and cons of ultra-high-field MRI/MRS for human application. Prog Nucl Magn Reson Spectrosc. 109 1-50. doi: 10.1016/j.pnmrs.2018.06.001

[3] Sarracanie M. and Salameh N Low-Field MRI: How Low Can We Go? A Fresh View on an Old Debate. Front. Phys. 8 (2020) 172. doi: 10.3389/fphy.2020.00172

[4] Liu, Y., Leong, A.T.L., Zhao, Y. Xiao L., Mak H.K.F., Chun On Tsang A., Lau G.K.K., Leung G.K.K., Wu E.X. A low-cost and shielding-free ultra-low-field brain MRI scanner. Nat Commun 12, (2021) 7238 https://doi.org/10.1038/s41467-021-27317-1).

[5] McDermott R., Lee S., Haken ten B., Trabesinger A.H., Pines A., Clarke J. Microtesla MRI with a superconducting quantum interference device. Proc Natl Acad Sci USA. 101 (2004) 7857–61. doi: 10.1073/pnas.0402382101.

[6] Clarke J., Hatridge M., Mößle M. SQUID-detected magnetic resonance imaging in microtesla fields. Annu Rev Biomed Eng. 9 (2007) 389–413. doi: 10.1146/annurev.bioeng.9.060906.152010.

[7] Espy M.A., Magnelind P.E., Matlashov A.N., Newman S.G., Sandin H.J., Schultz L.J., Urbaitis A.V., Vologov P. Progress toward a deployable SQUID-based ultra-low field MRI system for anatomical imaging. IEEE Trans Appl Supercond. 25 (2015) 1–5. doi: 10.1109/TASC.2014.2365473

[8] Colegrove, F. D., L. D. Schearer, and G. K. Walters. Polarization of He 3 gas by optical pumping. Physical Review 132.6 (1963): 2561. Doi:10.1103/PhysRev.132.2561

[9] Walker, Thad G., and William Happer. Spin-exchange optical pumping of noble-gas nuclei. Reviews of modern physics 69.2 (1997): 629. doi:10.1103/RevModPhys.69.629

[10] Bowers, C. Russell, and Daniel P. Weitekamp. Transformation of symmetrization order to nuclear-spin magnetization by chemical reaction and nuclear magnetic resonance. Physical Review Letters 57.21 (1986): 2645. doi:10.1103/PhysRevLett.57.2645

[11] Dzien P., Kettunen M.I., MarcoRius I., Serrao E.M., Rodrigues T.B., Larkin T.J., Timm K.N., Brindle K.M. 13C magnetic resonance spectroscopic imaging of hyperpolarized [1-13C, U-2H5] ethanol oxidation can be used to assess aldehyde dehydrogenase activity in vivo. Magnetic Resonance in Medicine 73.5 (2015): 1733-1740. doi:10.1002/mrm.25286

[12] Sushentsev N., McLean M.A., Warren A.Y., Benjamin A.J.V., Brodie C., Frary A., Gill A.B., Jones J., Kaggie J.D., Lamb B.W., Locke M.J., Miller J.L., Mills I.G., Priest A.N., Robb F.J.L., Shah N., Schulte R.F., Graves M.J., Gnanapragasam V., Brindle K.M., Barrett T., Gallagher F.A. Hyperpolarised $^{13}$C-MRI identifies the emergence of a glycolytic cell population within intermediate-risk human prostate cancer. Nat Commun. 24;13(1) (2022) 466. doi: 10.1038/s41467-022-28069-2

[13] Abragam A., Goldman M., Principles of dynamic nuclear polarisation, Rep. Prog. Phys. 41 (3) (1978) 395. doi:10.1088/0034-4885/41/3/002

[14] Lurie, D. J., Bussell, D. M., Bell, L. H., & Mallard, J. R. (1988). Proton-electron double magnetic resonance imaging of free radical solutions. Journal of Magnetic Resonance 76(2) (1988) 366-370. doi:10.1016/0022-2364(88)90123-0

[15] Yasukawa K, Hirago A, Yamada K, Tun X, Ohkuma K, Utsumi H. In vivo redox imaging of dextran sodium sulfate-induced colitis in mice using Overhauser-enhanced magnetic resonance imaging. Free Radic Biol Med. 20 (2019) 136:1-11. doi: 10.1016/j.freeradbiomed.2019.03.025.

[16] Golman K., Petersson J.S., Ardenkjaer-Larsen J.H., Leunbach I., Wistrand L.G., Ehnholm G., Liu K. Dynamic in vivo oxymetry using overhauser enhanced MR imaging. J Magn Reson Imaging. 12(6) (2000) 929-38. doi: 10.1002/1522-2586(200012)12:6<929::aid-jmri17>3.0.co;2-j.

[17] Matsumoto K, Subramanian S, Murugesan R, Mitchell JB, Krishna MC. Spatially resolved biologic information from in vivo EPRI, OMRI, and MRI. Antioxidants & redox signaling 9(8) (2007): 1125-1142. doi: 10.1089/ars.2007.1638. PMID: 17571957.

[18] Gorodetskii A.A., Eubank T.D., Driesschaert B., Poncelet M., Ellis E., Khramtsov V.V., Bobko A.A. Oxygen-induced leakage of spin polarization in Overhauser-enhanced magnetic resonance imaging: Application for oximetry in tumors. J Magn Reson. 297 (2018) 42-50. doi: 10.1016/j.jmr.2018.10.005.

[19] Waddington DEJ, Sarracanie M, Salameh N, Herisson F, Ayata C, Rosen MS. An Overhauser-enhanced-MRI platform for dynamic free radical imaging in vivo. NMR Biomed. 2018 May;31(5):e3896. doi: 10.1002/nbm.3896. Epub 2018 Mar 1. PMID: 29493032.

[20] López-Otín C., Bond JS. Proteases: multifunctional enzymes in life and disease. J Biol Chem. 2008 Nov 7;283(45):30433-7. doi: 10.1074/jbc.R800035200

[21] Yamaguchi H, Kimura T, Mimura K, Nawata H. Activation of proteases in cerulein-induced pancreatitis. Pancreas 4(5) (1989) 565-71. doi: 10.1097/00006676-198910000-00007.

[22] Sloane, B.F., List K., Fingleton B., Matrisian L. Proteases in cancer: significance for invasion and metastasis. in Proteases: structure and function. Springer, Vienna (2013). 491-550. https://doi.org/10.1007/978-3-7091-0885-7_15

[23] Madhusudhan T., Kerlin B.A., Isermann B.. The emerging role of coagulation proteases in kidney disease. Nature reviews nephrology 12(2) (2016): 94. doi: 10.1038/nrneph.2015.177

[24] Cunningham M.A., Rondeau E., Chen X., Coughlin S.R., Holdsworth S.R., Tipping P.G.. Protease-activated receptor 1 mediates thrombin-dependent, cell-mediated renal inflammation in crescentic glomerulonephritis. J Exp Med. 7;191(3) (2000) 455-62. doi: 10.1084/jem.191.3.455

[25] Birrer P., McElvaney N.G., Rüdeberg A., Sommer C.W., Liechti-Gallati S. Kraemer R., Hubbard R., Crystal R.G. Protease-antiprotease imbalance in the lungs of children with cystic fibrosis. Am J Respir Crit Care Med. 150(1) (1994) 207-13. doi: 10.1164/ajrccm.150.1.7912987.

[26] Shapiro, S. D. Proteinases in chronic obstructive pulmonary disease. Biochemical Society Transactions 30(2) (2002): 98-102. doi: 10.1042/bst0300098

[27] Rivot A., Jugniot N., Jacoutot S., Vanthuyne N., Massot, P., Mellet P., Marque S.R. A, Audran G., Voisin P., Delles M., Devouassoux G., Thiaudiere E., Bentaher A., Parzy E. Magnetic Resonance Imaging of Protease-Mediated Lung Tissue Inflammation and Injury. ACS Omega 6:23 (2021) 15012–15016. doi.org/10.1021/acsomega.1c01150

[28] Audran G., Bosco L., Brémond P., Franconi J.M., Koonjoo N., Marque S.R., Massot P., Mellet P., Parzy E., Thiaudière E. Enzymatically Shifting Nitroxides for EPR Spectroscopy and Overhauser-Enhanced Magnetic Resonance Imaging. Angew Chem Int Ed Engl. 54:45 (2015) 13379-84. 10.1002/anie.201506267

[29] International Commission on Non-Ionizing Radiation Protection. Guidelines for limiting exposure to time-varying electric, magnetic, and electromagnetic fields (up to 300 GHz). Health physics 74(4) (1998): 494-522.

[30] Wald LL, McDaniel PC, Witzel T, Stockmann JP, Cooley CZ. Low-cost and portable MRI. J Magn Reson Imaging. 52(3) (2020) 686-696. doi: 10.1002/jmri.26942

[31] Parzy, E., et al. Enzymatic activity monitoring through dynamic nuclear polarization in Earth magnetic field. J.Magn Reson 333 (2021): 107095.

[32] GuiberteauT. Grucker D. EPR spectroscopy by dynamic nuclear polarization in low magnetic field. Journal of Magnetic Resonance, Series B 110.1 (1996): 47-54. https://doi.org/10.1006/jmrb.1996.0006

[33] Lother S., Hoelscher U., Kampf T., Jakob P., Fidler F. 3D gradient system for two B0 field directions in earth's field MRI. MAGMA. 26(6) (2013) 565-73. doi: 10.1007/s10334-013-0376-5

[34] Massot P., Parzy E., Pourtau L., Mellet P., Madelin G., Marque S., Franconi J.M., Thiaudiere E.. In vivo high-resolution 3D overhauser-enhanced MRI in mice at 0.2 T. Contrast Media Mol Imaging. 7(1) (2012) 45-50. doi: 10.1002/cmmi.464

[35] Zotev V.S., Volegov P.L., Matlashov A.N., Savukov I.M., Owen T., and Espy M.A. SQUID-based microtesla MRI for in vivo relaxometry of the human brain. IEEE Transactions on Applied Superconductivity 19(3) (2009): 823-826. doi: 10.1109/TASC.2009.2018764

[36] Zhu, B., Liu, J., Cauley, S.F, Rosen B.R., Rosen M.S. Image reconstruction by domain-transform manifold learning. Nature 555 (2018) 487–492. https://doi.org/10.1038/nature25988

[37] Ayde, R., Senft, T., Salameh, N., & Sarracanie, M. Deep learning for fast low-field MRI acquisitions. Scientific reports, 12(1) (2022) 1-13.

[38] Froidevaux, R., Weiger, M., Brunner, D. O., Dietrich, B. E., Wilm, B. J., Pruessmann, K. P. Filling the dead-time gap in zero echo time MRI: Principles compared. Magnetic Resonance in Medicine, 79(4) (2018). 2036-2045. doi:10.1002/mrm.26875

[39] Faber P. and Garby L. Fat content affects heat capacity: a study in mice. Acta Physiol Scand 153 185-187. (1995) doi:10.1111/j.1748-1716.1995.tb09850.x

[40] N. Jugniot, I. Duttagupta, A. Rivot, P. Massot, C. Cardiet, A. Pizzoccaro, M. Jean, N. Vanthuyne, J.M. Franconi, P. Voisin, G. Devouassoux, E. Parzy, E. Thiaudiere, S.R.A. Marque, A. Bentaher, G. Audran, P. Mellet, An elastase activity reporter for Electronic Paramagnetic Resonance (EPR) and Overhauser-enhanced Magnetic Resonance Imaging (OMRI) as a line-shifting nitroxide, Free Radic. Biol. Med. 126 (2018) 101–112, https://doi.org/10.1016/j. freeradbiomed.2018.08.006.

[41] Couet, W.R., Eriksson U.G., Tozer T.N., Tuck L.D., Wesbey G.E., Nitecki D., Brasch, R.C. Pharmacokinetics and metabolic fate of two nitroxides potentially useful as contrast agents for magnetic resonance imaging. Pharm. Res. 1(5) (1984) 203-9. doi: 10.1023/A:1016317212601.

[42] Khramtsov V.V., Zweier J.L., Functional in vivo EPR Spectroscopy and Imaging Using Nitroxide and Trityl Radicals, Stable. Radicals: Fundamentals and Applied Aspects of Odd-Electron Compounds (Ed.: R. G. Hicks), Wiley, Chichester (2010) 537–566. doi.org/10.1002/9780470666975.ch16

# 3D-MRI @ 8.5 kHz

20 mT → 200 µT

EPR @ 72 kHz

Free Radical

200 µT